

Research Article

Accurate large scale modelling of graphene oxide: Ion trapping and chaotropic potential at the interface

Mohamed Ali al-Badri ^{a, **}, Paul Smith ^a, Robert C. Sinclair ^b, Khuloud T. al-Jamal ^c, Christian D. Lorenz ^{a,*}

^a Department of Physics, King's College London, London, WC2R 2LS, UK

^b Centre for Computational Sciences, University College London, London, WC1H 0AJ, UK

^c Institute of Pharmaceutical Science, King's College London, London, SE1 9NH, UK

ARTICLE INFO

Article history:

Received 21 October 2020

Received in revised form

9 December 2020

Accepted 10 December 2020

Available online 16 December 2020

Keywords:

Molecular dynamics simulations
Bespoke quantum derived forcefield
Graphene oxide
Interfacial phenomena

ABSTRACT

Graphene oxide (GO) shares many novel mechanical and electronic properties with graphene and has been applied extensively for uses in physics, engineering and medicine. Computational simulations of GO have widely neglected accurate characterisation by random functionalisation, forsaking steric strain and abandoning edge functional groups. Here, we show that molecular dynamics forcefield design using electronic structure calculations of hundreds of atoms of GO with accurate functionalisation shows good agreement with state-of-the-art *ab initio* molecular dynamics (AIMD) simulations. We find that the bespoke forcefield shows better agreement with previous AIMD and experimental results in terms of the interfacial water dynamics and ion adsorption. Namely, GO described by the bespoke forcefield is found to disrupt the hydrogen bonding network at the interface by playing a more dynamic role in accepting and donating hydrogen bonds from water. Furthermore, with the bespoke forcefield, we find preferential adsorption of ions to carboxyl functional groups and a similar mean adsorption half-life for Na⁺ and Cl⁻ ions around GO. These findings are critical for future investigations of GO in complex environments in application ranging from desalination to protein adsorption for drug delivery.

© 2020 Elsevier Ltd. All rights reserved.

1. Introduction

Graphene oxide (GO) is an amorphous 2D material with complex chemistry and a diverse array of potential applications. GO can be difficult to characterise because of its irregular nature, myriad of functional groups, sensitivity to synthesis method, and high reactivity. This has lead to poor understanding in the literature and great difficulty in simulating GO with conflicting reports in experimental papers[1].

There is no precise consensus on the nanostructure of GO. The Lierf-Klinowski model [2] is widely recognised and has formed the basis of much scientific research [3,4]. Lierf and Klinowski identified the most common functional groups in graphene oxide: epoxy and alcohol groups on the surfaces, with alcohol and carboxyl groups around the edges. However, they assume no correlation between

the location of functional groups. Correlation between oxidised sites seems chemically intuitive when one considers isolated carbon double bonds are more reactive than conjugated/aromatic systems [5]; indeed, several experiments have shown the presence of oxidised and unoxidised regions[6–8].

Accurately describing the structure of GO is important, but one must also consider the forcefield used to describe it in a molecular dynamics (MD) simulation. Traditionally classical forcefields are parameterised for transferability, and are used to describe a large family of molecules[9–11]. More recently, generalised varieties of the CHARMM and AMBER forcefield have been used to generate, with minimal effort, parameters for an increasingly large number of molecules[11–13]. Previously, MD has been used to study the interactions of GO with ionic solutions[14], water[15–18], gases [19,20], peptides [21,22] and lipid bilayers[23], in which parameters from these traditional families of force fields were used to approximate GO's chemical properties. As we find in our work, water structure is well described by generalised forcefields, requiring only an accurate representation of GO structure and allowing for structural flexibility. Such work has been recently

* Corresponding author.

** Corresponding author.

E-mail addresses: mohamed.al-badri@kcl.ac.uk (M.A. al-Badri), chris.lorenz@kcl.ac.uk (C.D. Lorenz).

applied to study the nanopore connectivity and swelling of GO with varying GO membrane separation and degree of oxidation, work that is vital to understand GO for applications in gaseous or aqueous separation[24,25].

The computational cost of electronic structure calculations is a bottleneck to accurate modelling of heterogeneous nanomaterials such as the two-phase or semi-ordered structure of GO. The semi-ordered structure of GO is defined as the inhomogeneous regions of oxidised and unoxidised domains, where amorphous alcohol and epoxy groups make up the oxidised regions. In contrast, random functionalisation assumes an uncorrelated random distribution of oxidised functional groups. Limitations on the size and conformation can be remedied by imposing periodic boundary conditions (thereby simulating an infinite sheet of GO) as well as planarity to the topology. However this neglects both the chemistry of aforementioned edge functional groups and capping hydrogen atoms and the structural deformation induced by steric effects from correlated oxidised sites.

Subasinghe Don et al. [26] and Mouhat et al. [27] have recently studied the structure of water at the interface of GO using state of the art *ab initio* molecular dynamics (AIMD) simulations. Subasinghe Don et al. [26] conducted NVT simulations to compare the performance of classical MD using the Optimized Potentials for Liquid Simulations All-Atom (OPLS-AA) forcefield to AIMD when modelling a single shell of water at the GO interface within the confines of a large cubic simulation box, mainly composed of a vacuum. This sandwiching vacuum biases water molecules towards the surface for adsorption and neglects the role of bulk water on water dynamics at the GO surface. Mouhat et al. [27] present an exceptional comparison of randomly functionalised and more realistic heterogeneous (semi-ordered) models of GO. Their results show that semi-ordered models of GO are the most stable structures in vacuum as well as in liquid water. Despite the accuracy of their realistic semi-ordered model, their work neglects the role of both carboxyl and phenol edge functional groups. We show that, even though they are much less prevalent than functional groups on the GO surface, edge groups play an important role in water and ion dynamics and should not be disregarded. To the best of our knowledge, the behaviour of semi-ordered GO in ionic solution is yet to be investigated using AIMD.

Accurate forcefields are paramount in bridging between experiment and engineering novel applications of graphitic materials, where atomic scale chemistry defines their macroscopic behaviour. In order to achieve this without the limitations on simulation time and system size, we propose an intermediate level of accuracy that advances on generalised forcefields through deriving non-bonded forcefield parameters from *ab initio* Density Functional Theory (DFT) calculations. This approach allows for the transferability of electronic structure calculations to a dynamic picture of GO at biologically relevant time scales (hundreds of nanoseconds) and systems composed of hundreds of thousands of atoms, as is the purview of MD.

In this study, we present novel electronic structure derived forcefield parameters using the Density Derived Electrostatic and Chemical partitioning method (DDEC) from DFT calculations. We use the DDEC derived forcefield to compare water dynamics in both aqueous and ionic solutions with that observed using the generalised OPLS forcefield.

2. Results

2.1. Forcefield parameters

The structure of the GO sheet is given in Fig. 1, where functional groups have been annotated according to the OPLS forcefield naming scheme used herein.

The DDEC and OPLS non-bonded forcefield parameters are presented in Fig. 2. There is a clear deviation from OPLS parameters for some atomic species, particularly significant in the partial charge distributions. The most notable finding in these distributions is the large variance in partial charge of many individual atomic species, including distributions that span either side of a charge of zero. Lennard-Jones parameters are derived from the DDEC charge density using the Tkatchenko-Scheffler relations[28], where ϵ values are mostly in the vicinity of OPLS-AA parameters, σ values however show a large deviation between the two approaches.

The lateral distribution of partial charges across the GO surface illustrates their variation and correlation with functionalised regions in Fig. 3. It displays the disparity between the two approaches, with a continuous DDEC charge distribution – representative of the DFT electrostatic density – in contrast to the constant OPLS charges that are distributed discretely. Furthermore, the DDEC GO surface carbon atoms have a variance in partial charge distribution spanning negative to positive charge, unlike OPLS which restricts all GO surface carbon atoms to either zero or positive partial charge.

2.1.1. Structural fluctuations

Previous studies using reactive forcefields [29], DFT [30] and AIMD [27] have found that the correlated environment of oxygen-bearing (alcohol and epoxy) functional groups in semi-ordered GO stabilise the edifice through intramolecular hydrogen bonds. In solution, the heterogeneous structure of GO induces structural deformation due to the steric effect of correlated epoxy and alcohol groups. We show that the deformation is similar for both DDEC and OPLS forcefields through the distance of each atom to the mean in the orthogonal plane (Fig. 4). Minute structural differences arise within correlated environments, due to the difference in the intramolecular hydrogen bonds between epoxy-epoxy and alcohol-alcohol groups in DDEC and OPLS. A larger number of intramolecular hydrogen bonds stabilise the local chemical environment to a greater degree in DDEC, reducing its perturbation away from the mean in the orthogonal plane.

Using a hydrogen-bond angle cut-off of 150° , the intramolecular hydrogen-bond of O1–O1 (alcohol-alcohol) and O2–O2 (epoxy-epoxy) is double and triple the prevalence in DDEC than in OPLS, respectively (Table 1).

2.2. Water structure

The radial distribution functions (RDFs) of the constituent GO atomic species with respect to the water oxygen atoms are shown in Fig. 5, along with their hydration numbers — the mean water count within the region enveloped by the first RDF minimum. The radial distribution function between atoms a and b is given by Eq. (1), with a radial cumulative distribution function $G_{ab}(r) = \int_0^r dr' 4\pi r'^2 g_{ab}$ where the average coordination number of b atoms at radius r is given by $N_{ab}(r) = \rho G_{ab}(r)$.

$$g_{ab}(r) = (N_a N_b)^{-1} \sum_{i=1}^{N_a} \sum_{j=1}^{N_b} \langle \delta(|\mathbf{r}_i - \mathbf{r}_j| - r) \rangle \quad (1)$$

The RDFs show that water oxygen atoms are more tightly bound to the GO oxygens than the GO carbon atoms, where the first water shell has a radius of approximately 4 Å and 5 Å, respectively. Water oxygen atoms show weak structuring around GO carbon atoms (Fig. 5B). Aromatic carbon atoms (C1) belonging to pristine (sp^2) graphene regions, show the weakest water structuring of all constituent atom types, noting that the weak structuring of water around the tertiary alkyl carbon (C2) atoms is due to their

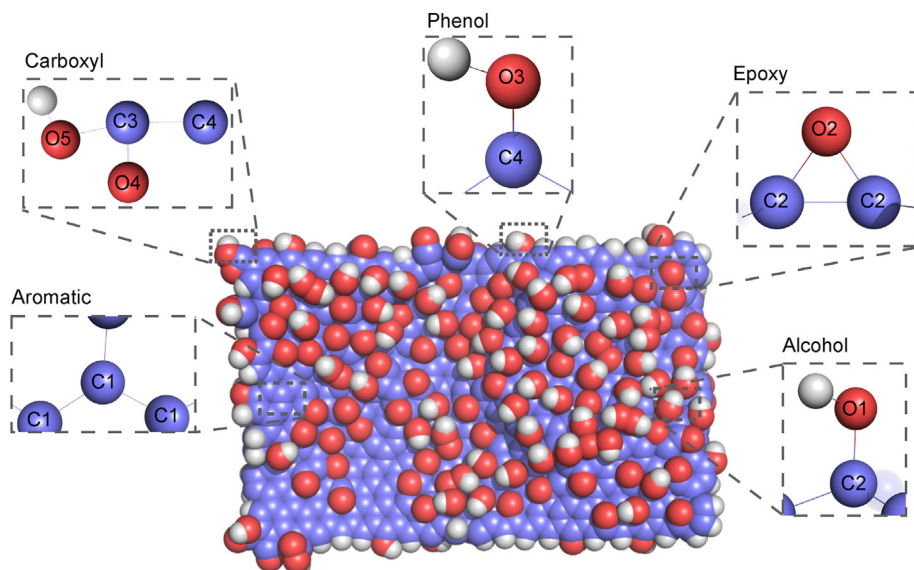


Fig. 1. The semi-ordered 979 atom GO sheet structure, showing regions of oxidised and unoxidised domains. Inset images highlight the structures and naming convention of aromatic carbon and alcohol, epoxy, phenol and carboxyl functional group atoms. (A colour version of this figure can be viewed online.)

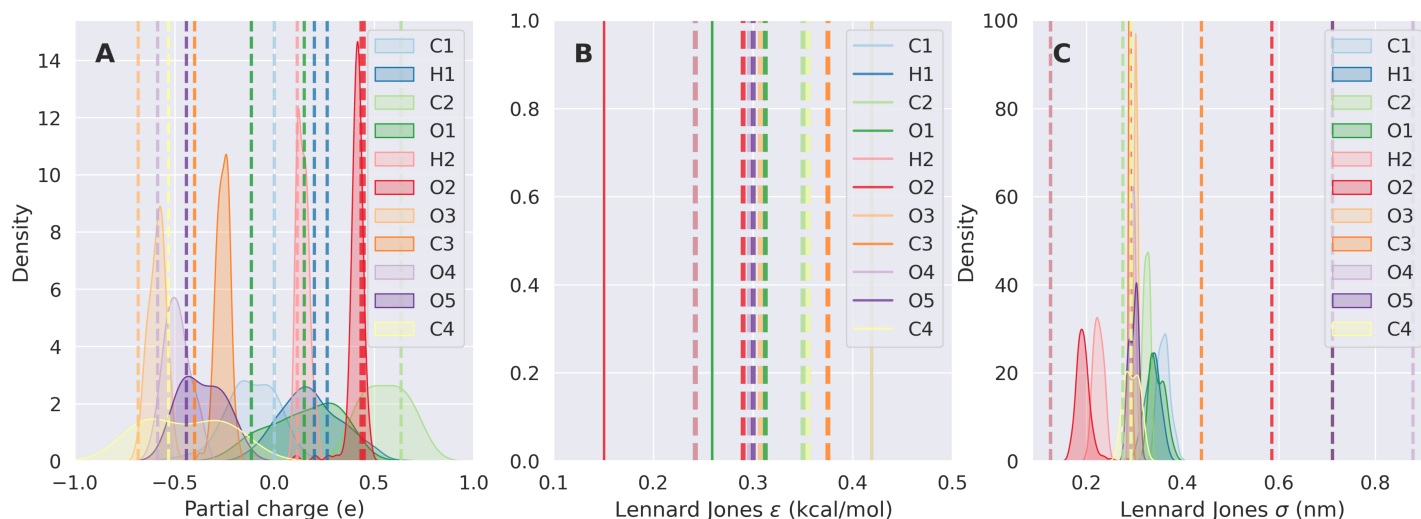


Fig. 2. The distribution of DDEC (A) partial charge, (B) Lennard Jones ϵ and (C) Lennard Jones σ non-bonded forcefield parameters for the component atom types of the GO sheet. OPLS parameters are presented as dashed lines. (A colour version of this figure can be viewed online.)

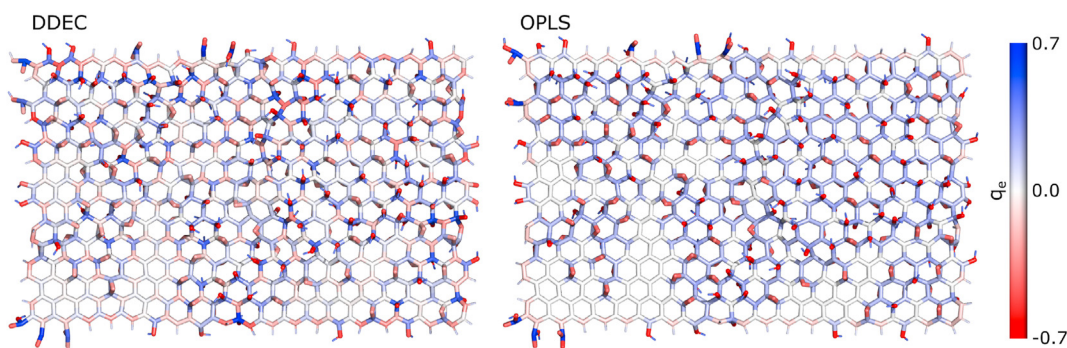


Fig. 3. The lateral illustration of OPLS and DDEC partial charges of the graphene-oxide sheet. (A colour version of this figure can be viewed online.)

coordination by an alcohol group. The water surrounding GO becomes representative of the bulk at 12 Å.

We observe a strong correlation (Pearson coefficient, $R = 0.98$) between the DDEC and OPLS forcefields when considering the

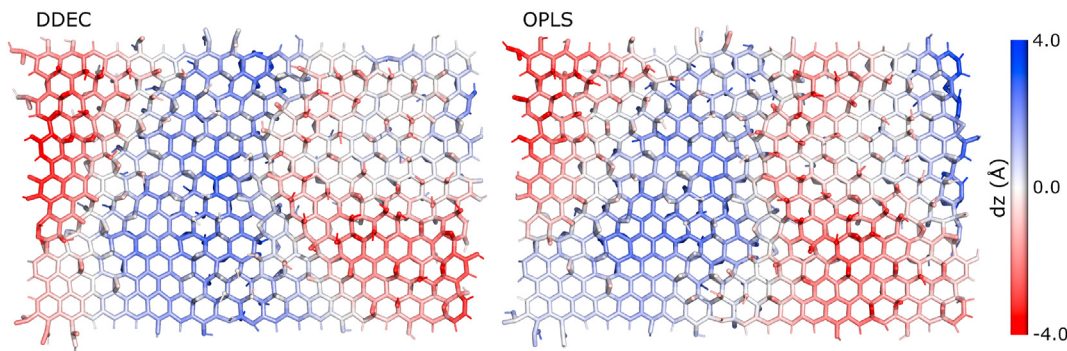


Fig. 4. The structural deformation of the GO sheet in solution, measured by the distance from the mean in the orthogonal plane for the duration of the MD simulation for DDEC (left) and OPLS (right) forcefields. (A colour version of this figure can be viewed online.)

Table 1

Mean number of intramolecular and intermolecular GO hydrogen bonds according to atom type for DDEC and OPLS GO, where the highest numbers of hydrogen bonds are highlighted. Intramolecular hydrogen bonds are normalised by the number of donor atoms. Water-GO hydrogen bonds are normalised by the number of GO atoms. Columns and rows denote accepting and donating species, respectively. Zero hydrogen bonds are denoted as dashes.

DDEC	OW	Alcohol O1	Epoxy O2	Phenol O3	Carboxyl O4	Carboxyl O5
OW		0.32	0.16	0.32	0.58	0.30
Alcohol O1	0.16	0.04	0.02	—	—	—
Phenol O3	0.24	0.01	—	—	—	—
Carboxyl O5	0.12	0.03	0.02	—	—	—
OPLS						
OW		0.36	0.26	0.51	0.57	0.22
Alcohol O1	0.11	0.02	0.01	—	—	—
Phenol O3	0.14	0.01	—	—	—	—
Carboxyl O5	0.14	—	—	—	—	—

mean number of hydrating water molecules around the individual atoms of the GO sheet in solution (Fig. 6A). Collectively, the structure of water as outlined by the atom-to-atom coordination correlation (Fig. 6A) and the RDFs and mean water count (Fig. 5) show a striking similarity between the two forcefields. In particular, this shows that the structure of water around a semi-ordered structure of GO is almost identical independent if it is described by the OPLS generalised forcefield or the bespoke *ab initio* forcefields, despite the variance within the forcefield parameters (Fig. 2).

In ionic solution, however, we find that the number of bound Na^+ and Cl^- ions is significantly different for the systems described by OPLS and by the DDEC forcefield. Further, there is little correlation between the two forcefields for sorption of the sodium ($R = 0.20$) (Fig. 6B) and chlorine ($R = 0.31$) (Fig. 6C) ions to specific atoms in the GO sheet. These disparities are the first signs that a bespoke forcefield parametrisation for exotic materials is necessary to describe the dynamics of GO in complex environments.

2.2.1. Interfacial water

Having established the effect of the local correlated chemical environment of the heterogeneous sheet on structural deformation and the different forcefields on the hydration of GO, we study the structure of water at the GO interface. As the GO sheet is flexible and dynamic, we cannot approximate its surface as a flat 2D sheet. Instead, we construct a discrete intrinsic surface based on the lateral xy coordinates of the GO carbon atoms. We linearly interpolate the intrinsic surface to provide a lateral resolution of $1.0 \times 1.0 \text{ \AA}^2$. In order to calculate the orientation of water with respect to the surface, we first define surface normals on a per-carbon atom basis then find the angle between the dipole moment of a water molecule and the normal of its nearest carbon atom. The normal to a carbon atom is estimated through a local least squares fitting of the plane formed by the atom and those

carbon atoms to which it is covalently bonded. To obtain the surface normal, we use the singular value decomposition (SVD) of the 3D coordinates of the carbon atoms:

$$A = U\Sigma V^T \quad (2)$$

where A is the matrix of 3D coordinates, Σ is a diagonal matrix of the singular values (in descending order), and U and V are orthogonal matrices that contain the left- and right-singular vectors of A , respectively. The normal to the surface is given by the right singular vector with the smallest corresponding singular value. As the SVD can not distinguish between a vector and its additive inverse, we take all normals to be oriented in the positive and negative z direction when considering water above and below the sheet, respectively.

To investigate the structure of water at the interface we report the density of water as a function of the distance in z from the intrinsic surface (Fig. 7A), defined by (Eq. (3)) [31]. Unlike the conventional mean density profile, the intrinsic density profile defines the instantaneous shape of a liquid surface as an intrinsic surface $z = \xi(x, y)$ where occupation histograms follow the contour of the instantaneous intrinsic surface for the GO conformation. Where $\xi(x, y)$ is the intrinsic surface for a given GO conformation for a cross-sectional area of the interface A_0 . The intrinsic density profile is given by:

$$\tilde{\rho}(z) = \langle \frac{1}{A_0} \sum_{i=1}^N \delta(z - z_i + \xi(x, y)) \rangle \quad (3)$$

The results of these measurements show that water above and below the GO sheet is almost symmetric in density — it is excluded at small distances before peaking at around 4 \AA (Fig. 7A), roughly the distance of the first minimum in the RDF (Fig. 5A). We see two

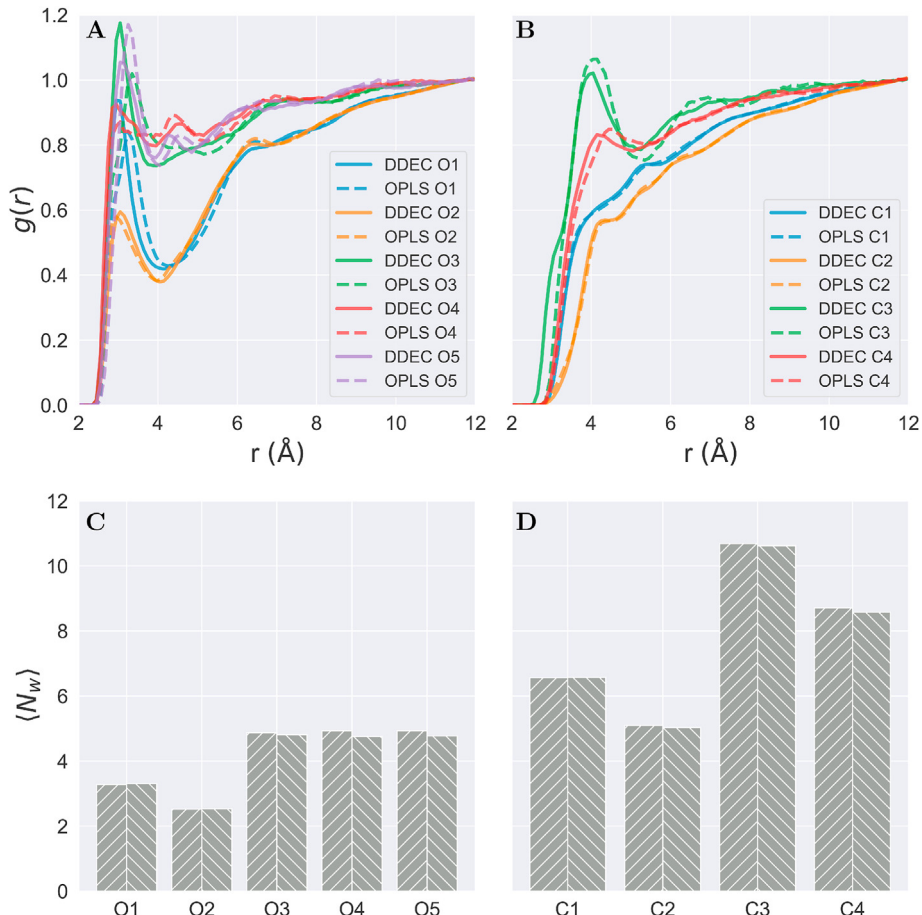


Fig. 5. The radial distribution functions of water oxygen atoms to the component GO (A) oxygen and (B) carbon atom types, according to both DDEC and OPLS forcefields and their respective hydration numbers for (C) oxygen and (D) carbon atom types. (A colour version of this figure can be viewed online.)

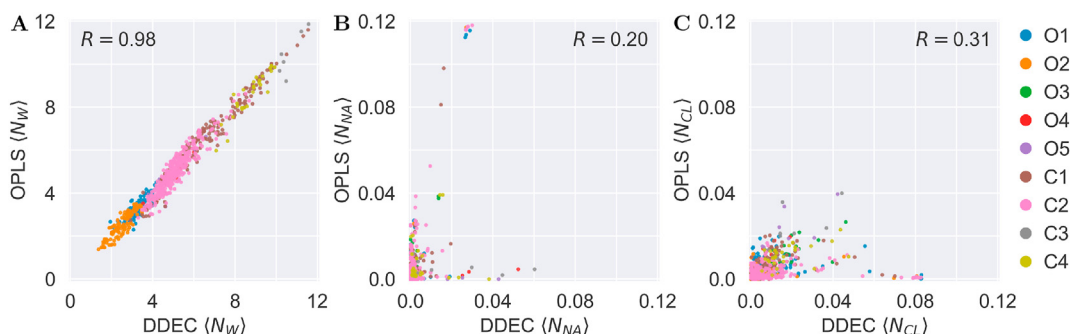


Fig. 6. The correlation of GO atom coordination number by (A) water molecules, (B) Na^+ and (C) Cl^- ions between the OPLS and DDEC forcefields, labeled by atom type. (A colour version of this figure can be viewed online.)

further hydration shells, but at longer distances than the first shell the water quickly becomes more bulk-like.

The mean number of water-water hydrogen bonds as a function of distance z from the intrinsic surface is given by:

$$\langle N_{HB}(z) \rangle = \left\langle \sum_{i=1}^N N_{HB,i} \delta(z - z_i + \xi(x, y)) \right\rangle \quad (4)$$

Using this as a metric, we see a disruption of the water hydrogen bond network by GO at small distances (Fig. 7B). This may be due to the formation of GO-water hydrogen bonds at the interface (Table 1). GO-water hydrogen bonds directly reduce the number of water-water hydrogen bonds, but may also require a reorientation

of water molecules at the interface, which would further disrupt the water hydrogen bond network.

The intrinsic orientational profile is defined by (Eq. 5), where $\hat{\mathbf{p}}_i$ is the unit vector pointing in the direction of the dipole moment of water, $\hat{\mathbf{n}}$ is the normal to the surface of the GO sheet [31].

$$\tilde{P}(z) = \frac{\hat{\mathbf{p}}_i \cdot \hat{\mathbf{n}}}{A_0} \sum_{i=1}^N \delta(z - z_i + \xi(x, y)) \quad (5)$$

In Fig. 7C, we see two preferred — and opposite — orientations of water within the first hydration shell. Water nearest the interface ($dz < 3.5 \text{ \AA}$) tends to be oriented with its hydrogen atoms near the

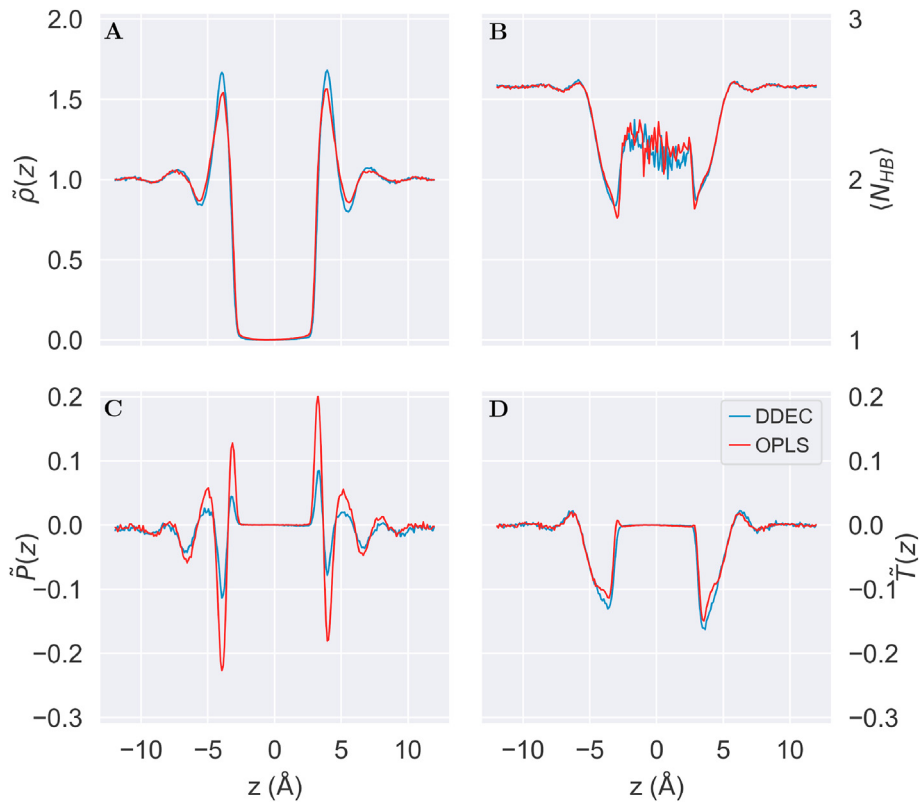


Fig. 7. Intrinsic structure of the GO-water interface for both OPLS and DDEC forcefields, as indicated by (A) the intrinsic density profile, normalised to its bulk value, (B) the number of water-water hydrogen bonds (N_{HB}), (C) the density-weighted profile of dipole orientation (\tilde{P}) and (D) the density-weighted intrinsic profile of the second moment of dipole orientation (\tilde{T}). (A colour version of this figure can be viewed online.)

GO sheet and oxygen atom facing the bulk ($\theta_{\mu_i} > 0$). The remainder of water within the first hydration shell ($3.5 \text{ \AA} < dz < 5 \text{ \AA}$) is oriented in the opposite direction, with the oxygen atom nearer the interface ($\theta_{\mu_i} < 0$). The two distinct orientations of water within the first hydration shell of the GO sheet may arise from water either donating or accepting hydrogen bonds with the polar atoms of GO.

The second moment distribution profile is defined by (Eq. (6)), and indicates whether the plane of a water molecule is oriented perpendicular ($\tilde{T} > 0$) or planar ($\tilde{T} < 0$) to the interface[31].

$$\tilde{T}(z) = \frac{(3\hat{\mathbf{p}}_i \cdot \hat{\mathbf{n}})^2 - 1}{2A_0} \sum_{i=1}^N \delta(z - z_i + \xi(x, y)) \quad (6)$$

In Fig. 7D, we see that water molecules tend to be oriented with both hydrogen atoms near the GO interface, rather than with one much nearer the interface than the other.

Fig. 7C suggests that water is more ordered at the GO interface in the OPLS system compared to the DDEC system. We now see this is indeed the case in the joint probability distribution $\rho(z, \theta_{\mu})$ of the dipole orientation at a distance z from the GO surface (Fig. 8). Generally, in the semi-ordered model of GO there is favourable orientation of water in the 45° – 135° region for either side of the GO sheet, with the preferred orientations creating a mirror image of water orientation across the GO sheet. The orientations in Fig. 8 are calculated with the same reference normal vector (z) and as such, angles above ($z > 0$) and below ($z < 0$) the sheet are offset by 180° from one another.

In order to highlight the differences between the dipole angle orientations between the forcefields, we calculate the joint probability density of the difference (DDEC–OPLS) in dipole angle

orientation (Fig. 8). The joint probability density signals the orientational freedom of water at the DDEC GO interface, which is clearly defined for the first interfacial layer from the GO surface. This is illustrated by the difference plot of DDEC – OPLS density, where there is a greater spread of points at a distance 4 \AA from the GO surface. This finding is in agreement with previous AIMD results [26], where water was similarly found to display much greater orientational freedom than that observed in OPLS. As such, DDEC GO increases the entropy of the system through interference with non-covalent intermolecular interactions and is therefore considered a chaotropic agent. This property can play a fundamental role and can have vast ramifications on the physics of GO in complex environments, including biomolecules. In proteins, chaotropic agents reduce the stability of the native state formed by water molecules by reducing the hydrophobic effect, leading to destabilisation or complete denaturing[32].

2.2.2. Ion adsorption

Previously, the mean ion count around the constituent species of GO were seen to be grossly disparate between the two forcefields (Fig. 6B and C), where we observed a low atom-to-atom correlation $R = 0.20$ for Na^+ and $R = 0.31$ for Cl^- in ionic solution. The disparities in ion adsorption on GO call for an accurate formulation of forcefields for exotic materials, while establishing their agreement with experiment. The radial distribution functions of ionic atoms highlight the different adsorption patterns around OPLS and DDEC GO (Figs. 9 and 10). The adsorption of Na^+ on the GO sheet oxygen bearing functional groups has a consistent radius for the first solvation shell, differing only in coordination numbers (Fig. 9C). The largest disparity between the OPLS and DDEC GO is that in the latter Na^+ ions preferentially coordinate and are much more tightly

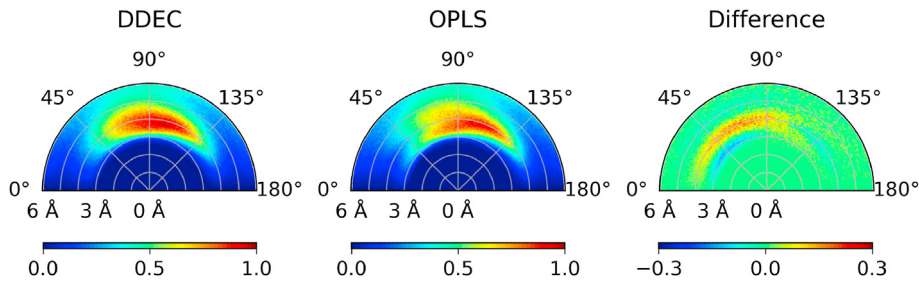


Fig. 8. The joint probability density $\rho(z, \theta_\mu)$ of the water dipole angle θ_μ as a function of z from the intrinsic surface of the GO sheet in solution, for both DDEC and OPLS forcefields. The difference plot shows $\rho^{\text{DDEC}}(z, \theta_\mu) - \rho^{\text{OPLS}}(z, \theta_\mu)$.

bound to edge carboxyl group atoms (carboxyl C3, carboxyl ketone O4 and carboxyl alcohol O5). This preferential adsorption of Na^+ ions to DDEC GO edge functional groups translates to an adsorption half life of 30–40 ps (Tables 2 and 3), highlighting the role of carboxyl groups in trapping Na^+ ions. This result is corroborated by the enhanced desalination performance of carboxyl functionalised GO when compared with pristine GO in experiment[33]. Instead, OPLS GO weakly coordinates Na^+ on edge carboxyl groups at larger distances, with well-ordered peaks in the RDF at 6–8 Å. In both forcefields, pristine graphene regions composed of aromatic carbons (C1) show diffuse and weak coordination of Na^+ , indicating that non-functionalised regions in semi-ordered GO sheets do not play a role in the trapping of Na^+ ions (Fig. 9B). Due to the constant

partial charge in all of the OPLS GO atoms, the binding of Na^+ ions to OPLS GO is predictable and wholly dependent on whichever component atoms have a negative partial charge, hence the strong coordination of Na^+ ions to alcohol, epoxy and phenol oxygen atoms as well as carboxyl carbon atoms (Fig. 9C and D).

Cl^- ions consistently adsorb to GO oxygen atoms at larger radii than Na^+ for both forcefields (Fig. 10A). Cl^- adsorption on OPLS and DDEC GO oxygen bearing functional groups have similar coordination numbers; favouring adsorption to alcohol oxygen (O1) and edge phenol group atoms (C4 and O3) in DDEC GO. In OPLS, however, Cl^- preferentially adsorbs to edge carboxyl alcohol oxygen (O5), followed by weaker coordination to edge phenol oxygen (O3) (Fig. 10A,C). Despite weak Cl^- adsorption to GO carbon atoms, it is

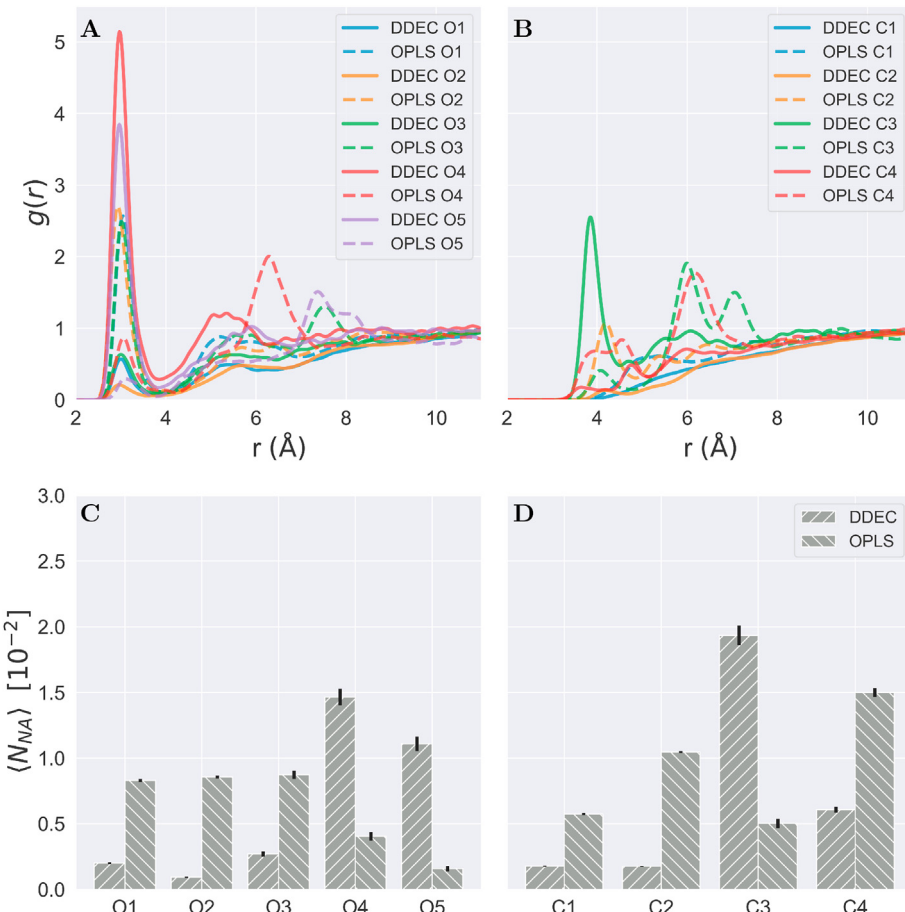


Fig. 9. The radial distribution functions of sodium ions to the component GO (A) oxygen and (B) carbon atom types, according to both DDEC and OPLS forcefields and their respective mean coordination numbers for (C) oxygen and (D) carbon atom types. Error bars indicate the standard error of the mean. (A colour version of this figure can be viewed online.)

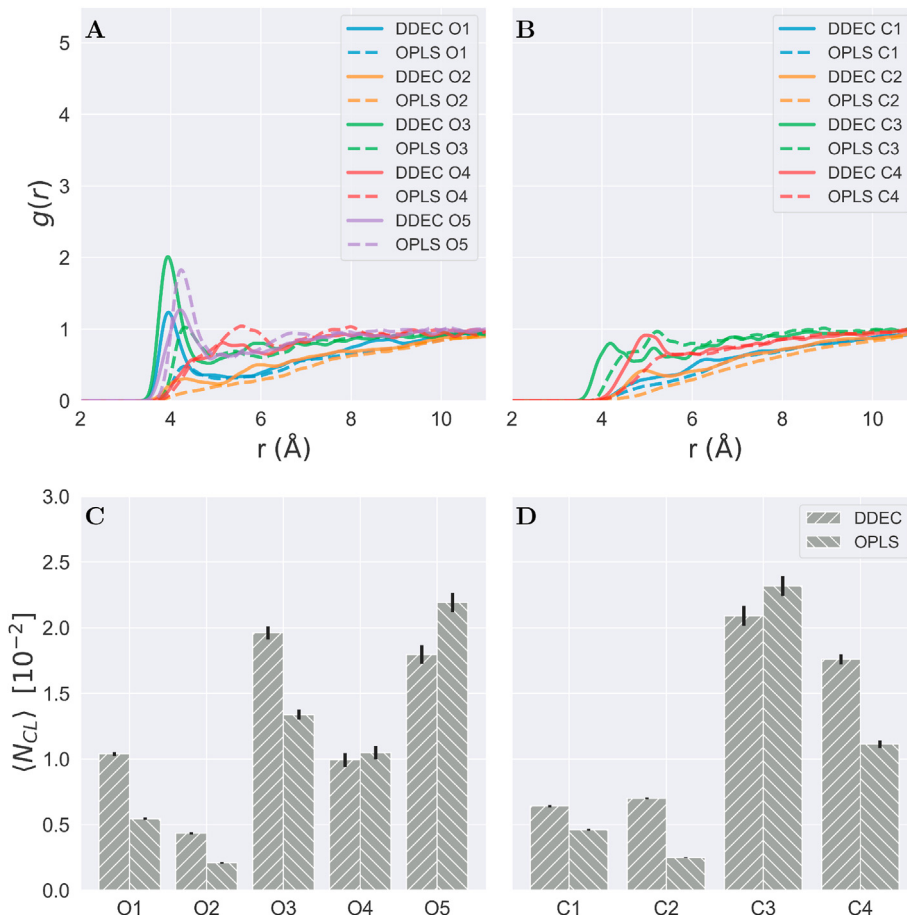


Fig. 10. The radial distribution functions of chlorine ions to the component GO (A) oxygen and (B) carbon atom types, according to both DDEC and OPLS forcefields and their respective mean coordination numbers for (C) oxygen and (D) carbon atom types. Error bars indicate the standard error of the mean. (A colour version of this figure can be viewed online.)

Table 2

Adsorption half-life (ps) of ion atoms around each GO carbon type.

	Aromatic C1	Tertiary alkyl C2	Carboxyl C3	Phenol C4
Na - DDEC	4.3	12.2	37.3	16.4
Na - OPLS	10.3	67.8	11.1	42.5
Cl - DDEC	8.9	15.1	12.0	8.4
Cl - OPLS	4.6	4.1	6.1	4.3

consistently more proximal in DDEC GO (Fig. 10B). Unlike Na^+ ions, the adsorption pattern of Cl^- ions is not significantly disparate to translate to a high variance in the adsorption half-life (Tables 2 and 3).

The survival probability of adsorbed ions at the first RDF minimum for each ion type is calculated using the self-diffusion tensor. Using this, virtual boundary conditions are imposed on the molecular system and survival probabilities and specified time correlation functions of the fluid are computed up to and including the interfacial layer, as proposed by Liu et al. [34] and implemented

using MDAnalysis [35,36]. The adsorption half-life is in turn computed by fitting the survival probability to a bi-exponential function in time[37], the results of which are presented in Tables 2 and 3. In order to accurately capture the ultrafast dynamics of ions, the coordinates of the MD trajectory were printed every ps for this analysis.

Using the adsorption half-life of the ions reported in Tables 2 and 3, the OPLS GO mean adsorption half-life over all atoms is 30.7 for Na^+ and 5.9 ps for Cl^- . For DDEC GO the mean adsorption half-life is 18.5 ps for Na^+ and 12.6 ps Cl^- , which is in agreement with experimental desalination studies to investigate ion rejection and permeation rates in GO, which find that Na^+ and Cl^- ions permeate at the same order of magnitude[38].

3. Conclusions

This work provides a framework for simulating graphitic materials, with an accuracy near that obtained with AIMD, while being able to study the dynamics of a system composed of hundreds of

Table 3

Adsorption half-life (ps) of ion atoms around each GO oxygen type.

	Alcohol O1	Epoxy O2	Phenol O3	Carboxyl ketone O4	Carboxyl alcohol O5
Na - DDEC	9.9	9.7	6.8	28.3	41.8
Na - OPLS	41.7	64.7	23.4	8.6	6.3
Cl - DDEC	22.1	16.3	12.5	6.6	11.4
Cl - OPLS	8.7	7.0	6.2	4.4	8.1

thousands of atoms for hundreds of nanoseconds. It extends on pre-existing generalised forcefields (OPLS-AA) and is solely designed to give accessibility to computationally investigate systems that are otherwise not well parameterised for molecular dynamics simulations, as is often the case for exotic materials. It is important to stress that the DDEC non-bonded forcefield parameters derived here are specific to a DFT calculation of the structure in question — a GO sheet with a different distribution of functional groups would require reparameterisation. In the case of no accurate generalised forcefield being available, software is required to apply this framework at scale to streamline the workflow from structure generation, to electronic structure calculation and finally to producing the forcefield files.

By using electronic structure calculations to derive non-bonded forcefield parameters, the MD simulations of a ~ 1000-atom GO sheet in solution shows that generalised forcefields are incredibly accurate at representing water structure around GO. However, GO in a complex environment — where strong electrostatic interactions with polar or charged moieties are present — ceases to be well described using generalised forcefields. It instead requires *ad hoc* parametrisation, at least until a definitively accurate empirical potential has been designed. Using the *ad hoc* forcefield, our analysis of the structure and dynamics of water near GO revealed a rotational freedom of water molecules within the first hydration shell not present in the generalised forcefield description of GO. The rotational freedom is concomitant with the flexible accepting and donating of hydrogen bonds between GO and water, allowing GO to disrupt the water hydrogen bonding network and acting as a chaotropic agent. Furthermore, when using the *ad hoc* forcefield we observe that the adsorption of Na^+ and Cl^- ions to GO, as described by RDFs, coordination and adsorption half-life, is affected by ion trapping by GO functional groups, which we do not observe to the same degree when employing the OPLS forcefield. This result is consistent with previous experimental findings. The ability of the *ad hoc* forcefield to capture these differences in the interfacial properties of an ionic solution with GO materials will undoubtedly be important in future investigations of the interaction of GO materials with saline solutions in applications like desalination and with biological molecules for its use in drug delivery formulations.

4. Methods

4.1. Geometry

We have modified a Python package [39] to generate rectangular graphene-oxide flakes. The package improves on the commonly applied protocol, discussed above, of randomly placing oxidised functional groups, which we now know is an incomplete model of graphene-oxide structure. Instead, we recreate the two-phase nature of oxidised and unoxidised graphene domains observed in microscopy experiments [6–8,40]. This approach has previously been revealed in a paper by Sinclair et al. [41], where the location of oxygen containing functional groups is determined by the reactivity possible oxidation sites. Using reactivities calculated by Yang et al. [42], successive oxidised groups can be added to the graphene skeleton in a realistic fashion. In this way, an accurate structure of graphene-oxide, with separate aromatic and highly oxidised domains, can be produced.

The output geometry was minimised using the OPLS molecular dynamics forcefield [43]. OPLS is a versatile forcefield which has been used for similar studies [44]. Minimising the structure in this way prior to performing electronic structure calculations enables the classical forcefield to optimise the approximate geometry generated by the Python package, and inherit the structural characteristics induced by explicit solvation. Hence reducing electrostatic artefacts to

an electronic structure calculation performed *in vacuo*, as previously applied and suggested by Lever et al. [45].

4.2. Molecular dynamics

All MD simulations were performed in GROMACS version 2020.1 on the ARCHER Cray XC30 supercomputer on a single 2.7 GHz, 12-core E5-2697 v2 (Ivy Bridge) series processor node. The all-atom OPLS forcefield was used to simulate the classical simulations, and replaced with DDEC non-bonded parameters where indicated. A position restraint algorithm was applied to all non-solvent atoms during equilibration. The ~80 Å cubic simulation box was fully solvated with TIP3P water molecules. The system was relaxed energetically using steepest-descent energy minimisation for 50,000 steps with an energetic step size of 0.01 kJ/mol. The minimisation was terminated after the maximum energetic contribution was lower than a threshold of 1000.0 kJ/mol/nm. NVT and NPT equilibration was performed for 100 ps using two separate velocity-rescaling thermostat coupling temperature to velocities for graphene and solvent molecules (NVT), where a temperature of 300 K was maintained and 1 bar using the Parrinello-Rahman barostat (NPT). The Verlet cut-off scheme was employed to generate pair lists and the electrostatic interactions were calculated using the Particle-Mesh Ewald algorithm. Both electrostatic and van der Waals interactions were cut off beyond 1.2 nm. All bonds involving hydrogen atoms were constrained using the LINCS algorithm. Production simulations were run for 60 ns using a timestep of 1 fs. Analysis was performed using the MDAnalysis package [35,36,46]. All results presented in the text are for GO in pure TIP3P water, unless it is explicitly stated that they are from the simulation we performed with GO in 150 mM (0.15 mol/L) NaCl solution. Note that the results of our analysis of the water dynamics are indistinguishable between the two solutions.

4.3. DFT

The DFT ground-state was obtained using ONETEP [47], which is a linear-scaling DFT code that is formally equivalent to a plane-wave method. Linear-scaling can be achieved by the *in situ* variational optimisation of its atom-centered basis set (spatially-truncated nonorthogonal generalised Wannier functions, or NGWFs) [48]. The total energy is directly minimised with respect to the NGWFs and the single-particle density matrix. The use of a minimal, optimized Wannier function representation of the density-matrix allows for the DFT ground state to be solved with relative ease in large systems. This is particularly useful in molecules, since explicit truncation of the basis functions ensures that the addition of vacuum does not increase the computational cost [49]. The spin-polarised DFT calculations of the 979 atom graphene-oxide system were run with an energy cut-off of 800 eV, using the Perdew-Burke-Ernzerhof (PBE) exchange-correlation functional [50]. Four NGWFs were employed on each of the carbon atoms and oxygen atoms, and one on each hydrogen. NGWFs were truncated using 11 Å cutoff radii. DFT calculations simulated the GO system *in vacuo*, without the explicit treatment of solvent molecules. The pseudopotentials were generated with the OPIUM pseudopotential generation project [51].

Finite-temperature DFT calculations using ensemble density functional theory (EDFT) [52–54] were used to simulate the graphene-oxide sheet containing 979 atoms. Within this formalism, ONETEP minimises the Helmholtz free energy functional to self-consistently find the KS states and their fractional occupancies, which are determined in the Fermi–Dirac [53] scheme using a smearing width $k_B T$ of the Fermi Dirac distribution of $T = 300$ K. The rate of convergence and the search for the electronic ground state using EDFT calculations can be expedited by imposing a kinetic energy

preconditioner of 2.5 Bohr. This works by removing the effect of the kinetic energy operator for high energy states, reducing the width of the eigenspectrum by making the high energy states more degenerate while leaving the low energy states unchanged[55].

4.3.1. DDEC

The DDEC module implemented in ONETEP was used to partition the electron density and assign atom-centered point charges and atomic volumes, it combines two Atoms In Molecule (AIM) approaches – iterative Hirshfeld (IH) and iterated stockholder atoms (ISA) – to assign atomic charges from the electron density. No off-center charges were used in this study. Electron density partitioning was performed using an IH to ISA ratio of 0.02. Lennard-Jones parameters were calculated using the Tkatchenko-Scheffler relations [28] using protocols previously adopted by Cole et al. [49] through the QUBEKit program as an application programming interface [56].

Code availability

A repository containing code and instructions for generating GO sheets is available from <https://github.com/maalbadri/Accurate-large-scale-modelling-of-GrapheneOxide>.

CRediT authorship contribution statement

Mohamed Ali al-Badri: Conceptualization, Methodology, Software, Validation, Formal analysis, Investigation, Writing - original draft, Visualization. **Paul Smith:** Methodology, Software, Validation, Formal analysis, Visualization. **Robert C. Sinclair:** Methodology, Software. **Khuloud T. al-Jamal:** Supervision. **Christian D. Lorenz:** Conceptualization, Writing - review & editing, Supervision, Resources.

Declaration of competing interest

The authors declare that they have no known competing financial interests or personal relationships that could have appeared to influence the work reported in this paper.

Acknowledgement

M.A.B acknowledges Dr. Edward B. Linscott, Dr. Daniel J. Cole and Prof. Arash Mostofi for helpful discussions. This work was supported by BBSRC (grant BB/M009513/1) and EPSRC (grant EP/N509498/1). Via our membership of the UK's HEC Materials Chemistry Consortium, which is funded by EPSRC (EP/L000202, EP/R029431), this work used the ARCHER UK National Supercomputing Service (<http://www.archer.ac.uk>).

References

- [1] D.R. Dreyer, S. Park, C.W. Bielawski, R.S. Ruoff, *Chem. Soc. Rev.* 39 (2010) 228–240.
- [2] A. Lerf, H. He, M. Forster, J. Klinowski, *J. Phys. Chem. B* 102 (1998) 4477–4482.
- [3] C.-J. Shih, S. Lin, R. Sharma, M.S. Strano, D. Blankschtein, *Langmuir* 28 (2012) 235–241.
- [4] H. Dai, Z. Xu, X. Yang, *J. Phys. Chem. C* 120 (2016) 22585–22596.
- [5] M. Trömel, M. Russ, *Angew. Chem.* 99 (1987) 1037–1038.
- [6] D. Pacilé, J. Meyer, A. Fraile Rodríguez, M. Papagno, C. Gómez-Navarro, R. Sundaram, M. Burghard, K. Kern, C. Carbone, U. Kaiser, *Carbon* 49 (2011) 966–972.
- [7] W. Cai, R.D. Piner, F.J. Stadermann, S. Park, M.A. Shaibat, Y. Ishii, D. Yang, A. Velamakanni, S.J. An, M. Stoller, J. An, D. Chen, R.S. Ruoff, *Science (New York, N.Y.)* 321 (2008) 1815–1817.
- [8] S. Saxena, T.A. Tyson, E. Negusse, *J. Phys. Chem. Lett.* 1 (2010) 3433–3437.
- [9] W.L. Jorgensen, D.S. Maxwell, J. Tirado-Rives, *J. Am. Chem. Soc.* 118 (1996) 11225–11236.
- [10] J.A. Maier, C. Martinez, K. Kasavajhala, L. Wickstrom, K.E. Hauser, C. Simmerling, *J. Chem. Theor. Comput.* 11 (2015) 3696–3713.
- [11] K. Vanommeslaeghe, E. Hatcher, C. Acharya, S. Kundu, S. Zhong, J. Shim, E. Darian, O. Guvench, P. Lopes, I. Vorobiov, et al., CHARMM general force field: a force field for drug-like molecules compatible with the CHARMM all-atom additive biological force fields, *J. Comput. Chem.* 31 (2010) 671–690.
- [12] J. Wang, R.M. Wolf, J.W. Caldwell, P.A. Kollman, D.A. Case, *J. Comput. Chem.* 25 (2004) 1157–1174.
- [13] J. Wang, W. Wang, P.A. Kollman, D.A. Case, *J. Mol. Graph. Model.* 25 (2006) 247–260.
- [14] H. Dai, Z. Xu, X. Yang, *J. Phys. Chem. C* 120 (2016) 22585–22596.
- [15] N. Wei, C. Lv, Z. Xu, *Langmuir* 30 (2014) 3572–3578.
- [16] C.-J. Shih, S. Lin, R. Sharma, M.S. Strano, D. Blankschtein, *Langmuir* 28 (2012) 235–241.
- [17] J.A.L. Willcox, H.J. Kim, *ACS Nano* 11 (2017) 2187–2193.
- [18] R. Devanathan, D. Chase-Woods, Y. Shin, D.W. Gotthold, *Sci. Rep.* 6 (2016) 29484.
- [19] S. Jiao, Z. Xu, *ACS Appl. Mater. Interfaces* 7 (2015) 9052–9059.
- [20] W. Li, X. Zheng, Z. Dong, C. Li, W. Wang, Y. Yan, J. Zhang, *J. Phys. Chem. C* 120 (2016) 26061–26066.
- [21] X. Sun, Z. Feng, T. Hou, Y. Li, *ACS Appl. Mater. Interfaces* 6 (2014) 7153–7163.
- [22] L. Baweja, K. Balamurugan, V. Subramanian, A. Dhawan, *J. Mol. Graph. Model.* 61 (2015) 175–185.
- [23] N. Willems, A. Urizberea, A.F. Verre, M. Iliut, M. Lelimousin, M. Hirtz, A. Vijayaraghavan, M.S.P. Sansom, *ACS Nano* 11 (2017) 1613–1625.
- [24] C. Williams, P. Carbone, F. Siperstein, *Nanoscale* 10 (2018) 1946–1956.
- [25] C.D. Williams, P. Carbone, F.R. Siperstein, *ACS Nano* 13 (2019) 2995–3004.
- [26] V. Subasinghe Don, R. David, P. Du, A. Milet, R. Kumar, *J. Phys. Chem. B* 123 (2019) 1636–1649.
- [27] F. Mouhat, F.-X. Coudert, M.-L. Bocquet, *Nat. Commun.* 11 (2020) 1–9.
- [28] A. Tkatchenko, M. Scheffler, *Physical Review Letters*, vol. 102, Publisher: American Physical Society, 2009, 073005.
- [29] P.V. Kumar, N.M. Bardhan, G.-Y. Chen, Z. Li, A.M. Belcher, J.C. Grossman, *Carbon* 100 (2016) 90–98.
- [30] S. Zhou, A. Bongiorno, *Sci. Rep.* 3 (2013) 2484.
- [31] H. Martinez, E. Chacón, P. Tarazona, F. Bresme, *Proc. Math. Phys. Eng. Sci.* 467 (2011) 1939–1958.
- [32] G. Salvi, P.D.L. Rios, M. Vendruscolo, *Proteins: Struct. Function Bioinf.* 61 (2005) 492–499.
- [33] Y. Yuan, X. Gao, Y. Wei, X. Wang, J. Wang, Y. Zhang, C. Gao, *Desalination* 405 (2017) 29–39.
- [34] P. Liu, E. Harder, B. Berne, *J. Phys. Chem. B* 108 (2004) 6595–6602.
- [35] R.J. Gowers, M. Linke, J. Barnoud, T.J.E. Reddy, M.N. Melo, S.L. Seyler, D.L. Dotson, J. Domanski, S. Buchoux, I.M. Kenney, O. Beckstein, MDAnalysis: A Python package for the rapid analysis of molecular dynamics simulations, in: S. Benthal, S. Rostrup (Eds.), *Proceedings of the 15th Python in Science Conference, SciPy, Austin, TX, 2016*, pp. 98–105.
- [36] R. Araya-Secchi, T. Perez-Acle, S.-g. Kang, T. Huynh, A. Bernardin, Y. Escalona, J.-A. Garate, A.D. Martinez, I.E. Garcia, J.C. Saez, et al., *Biophys. J.* 107 (2014) 599–612.
- [37] F. Pedregosa, et al., *J. Mach. Learn. Res.* 12 (2011) 2825–2830.
- [38] Y.H. Cho, H.W. Kim, H.D. Lee, J.E. Shin, B.M. Yoo, H.B. Park, *J. Membr. Sci.* 544 (2017) 425–435.
- [39] Sinclair, R. C., 2020; <https://github.com/velocirobbie/make-graphitics>, Accessed: December 15, 2020.
- [40] K. Erickson, R. Erni, Z. Lee, N. Alem, W. Gannett, A. Zettl, *Adv. Mater.* 22 (2010) 4467–4472.
- [41] R.C. Sinclair, P.V. Coveney, *J. Chem. Inf. Model.* 59 (2019) 2741.
- [42] J. Yang, G. Shi, Y. Tu, H. Fang, *Angew. Chem. Int. Ed.* 53 (2014) 10190–10194.
- [43] W.L. Jorgensen, D.S. Maxwell, J. Tirado-Rives, *J. Am. Chem. Soc.* 118 (1996) 11225–11236.
- [44] N. Wei, C. Lv, Z. Xu, *Langmuir* 30 (2014) 3572–3578.
- [45] G. Lever, D.J. Cole, N.D.M. Hine, P.D. Haynes, M.C. Payne, *J. Phys. Condens. Matter* 25 (2013) 152101. Publisher: IOP Publishing.
- [46] P. Smith, R.M. Ziolek, E. Gazzarrini, D.M. Owen, C.D. Lorenz, *Phys. Chem. Chem. Phys.* 21 (2019) 9845–9857.
- [47] C.-K. Skylaris, P.D. Haynes, A.A. Mostofi, M.C. Payne, *J. Chem. Phys.* 122 (2005), 084119. Publisher: American Institute of Physics.
- [48] C.-K. Skylaris, A.A. Mostofi, P.D. Haynes, O. Diéguez, M.C. Payne, *Phys. Rev. B* 66 (2002), 035119. Publisher: American Physical Society.
- [49] D.J. Cole, J.Z. Vilseck, J. Tirado-Rives, M.C. Payne, W.L. Jorgensen, *J. Chem. Theor. Comput.* 12 (2016) 2312–2323.
- [50] J.P. Perdew, K. Burke, M. Ernzerhof, *Phys. Rev. Lett.* 77 (1996) 3865–3868. Publisher: American Physical Society.
- [51] A.M. Rappe, K.M. Rabe, E. Kaxiras, J.D. Joannopoulos, *Phys. Rev. B* 41 (1990) 1227–1230. Publisher: American Physical Society.
- [52] N.D. Mermin, *Phys. Rev.* 137 (1965) A1441–A1443. Publisher: American Physical Society.
- [53] N. Marzari, D. Vanderbilt, M.C. Payne, *Phys. Rev. Lett.* 79 (1997) 1337–1340. Publisher: American Physical Society.
- [54] C. Freysoldt, S. Boeck, J. Neugebauer, *Phys. Rev. B* 79 (2009) 241103. Publisher: American Physical Society.
- [55] A.A. Mostofi, P.D. Haynes, C.-K. Skylaris, M.C. Payne, *J. Chem. Phys.* 119 (2003) 8842–8848. Publisher: American Institute of Physics.
- [56] J.T. Horton, A.E.A. Allen, L.S. Dodda, D.J. Cole, *J. Chem. Inf. Model.* 59 (2019) 1366–1381. Publisher: American Chemical Society.